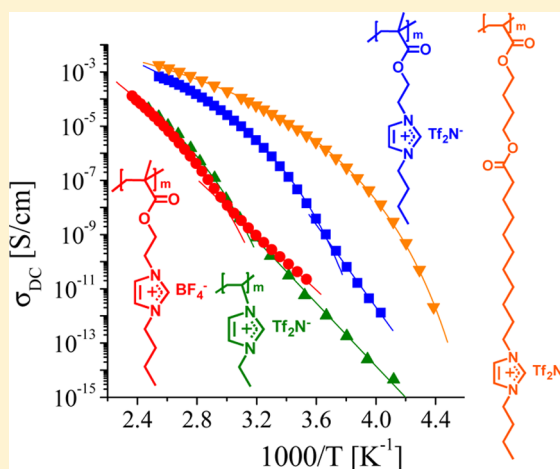


Dielectric and Viscoelastic Responses of Imidazolium-Based Ionomers with Different Counterions and Side Chain Lengths

U Hyeok Choi,[†] Yuesheng Ye,[‡] David Salas de la Cruz,[§] Wenjuan Liu,[†] Karen I. Winey,[§] Yossef A. Elabd,[‡] James Runt,[†] and Ralph H. Colby^{*,†}[†]Materials Science and Engineering, Pennsylvania State University, University Park, Pennsylvania 16802, United States[‡]Chemical and Biological Engineering, Drexel University, Philadelphia, Pennsylvania 19104, United States[§]Materials Science and Engineering, University of Pennsylvania, Philadelphia, Pennsylvania 19104, United States

S Supporting Information

ABSTRACT: A molecular-level understanding of dynamics in imidazolium-based ionomers with different counterions and side chain lengths was investigated using X-ray scattering, oscillatory shear, and dielectric relaxation spectroscopy (DRS). Variations of the counterion size and side chain length lead to changes in glass transition temperature (T_g), extent of ionic aggregation, and dielectric constant, with consequences for ion transport. A physical model of electrode polarization is used to determine the number density of simultaneously conducting ions and their mobility. Imidazolium-based ionomers with larger counterion and longer side chain have lower T_g , resulting in higher ionic conductivity and mobility. The ionic mobility is coupled to ion motions that are directly measured as a second segmental process in DRS, as these are observed to share the same Vogel temperature. Time–temperature superposition (tTS) was applied to create linear viscoelasticity master curves and to investigate the delay in chain motion related to ionic associations. tTS works well for these materials, and the terminal relaxation time increases with decreasing side chain length and smaller counterion size. X-ray scattering confirms the extent of ionic aggregation and helps to rationalize the observed dielectric constants. Larger counterions or longer side chains diminish ionic aggregation, and their ionomers have higher dielectric constants, which agree reasonably with the Onsager prediction at all temperatures studied. Smaller counterions or shorter side chains promote ionic aggregation, and their ionomers have lower dielectric constants, which are directly reflected in the lower content of simultaneously conducting ions.



■ INTRODUCTION

Ionic liquids (ILs) are composed entirely of large cations and anions with weak interactions and are highly advantageous because of their unique combination of physical properties including high thermal and chemical stability, negligible vapor pressure, broad electrochemical window, and high ionic conductivity.^{1–4} A common drawback to the use of ILs, however, is a concern about leakage of ILs in battery technology as well as in other organic electrolyte applications.¹ Hence, Ohno synthesized ILs with vinyl groups to facilitate preparation of polymerized ionic liquids (PILs), which carry an ionic liquid species in each repeating unit.^{5–16} The advantages of using PILs are enhanced stability, improved mechanical durability resulting from polymerization, and the simplification that only the counterions are able to move large distances rapidly. This makes PIL single-ion conductors ideal polymer electrolytes for advanced energy storage (batteries and supercapacitors), energy conversion (fuel cells), and electro-mechanical transduction devices (electroactive ionic actuators

and sensors). However, the ionic conductivity of ILs containing vinylimidazolium cations decreases considerably after polymerization due to an increase in the glass transition temperature (T_g)⁵ in addition to the severe restriction of cation mobility. It is therefore necessary to have a fundamental understanding of the relationships between chemical structure, morphology, and ion transport properties, which provide insights for the design of high-conductivity PIL single-ion conductors for diverse applications.

PILs derived from 1-alkyl-3-vinylimidazolium salts and their conducting properties were studied in 1998 by Ohno and Ito,⁵ and these materials have been extensively studied since.^{6,8–14,16–29} The pendant structures of these polymers were varied by introduction of polymerizable acrylate and methacrylate moieties; imidazolium units placed at the end of

Received: November 1, 2013

Revised: December 9, 2013

Published: January 6, 2014

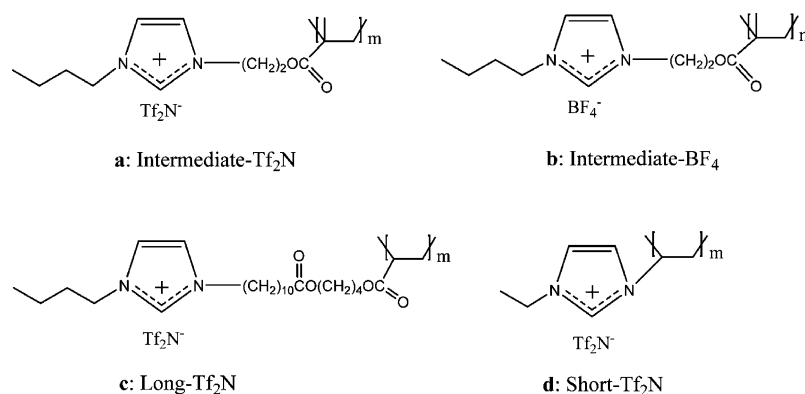


Figure 1. Chemical structures of imidazolium-based ionomers with (a) intermediate side chain with Tf₂N[−] counterion,²⁶ (b) intermediate side chain with BF₄[−] counterion,²⁶ and (c) longer side chain with Tf₂N[−] counterion.²⁹ The results from our ionomers are also compared with the earlier studies^{5,10,20,22,28} on ionomers with (d) shorter side chain with Tf₂N[−] counterion.

longer brush pendant chains afforded higher conductivities than shorter brush polymers.^{17,18} Elabd and co-workers¹⁹ investigated the effect of composition on ion conduction of random copolymers of imidazolium methacrylate and hexyl methacrylate. The copolymers displayed higher conductivity with high bis(trifluoromethylsulfonyl)imide (Tf₂N[−]) incorporation due to suppressed *T_g*, without microphase separation. Long and co-workers^{23,27} investigated the morphology and ionic conductivity of alkyl-substituted vinylimidazolium-based PILs as functions of alkyl chain length and counterion type. As the counterion size increased, regardless of alkyl substituent length, *T_g* decreased and ionic conductivity increased.

Nakamura et al.^{20,28,30} studied the dynamics of poly(1-ethyl-3-vinylimidazolium)-based PILs with various counterions using dielectric and viscoelastic measurements. For these PILs, conductivity and a relaxation process associated with ion pair motion displayed Arrhenius temperature dependence at temperatures below *T_g* and become stronger and non-Arrhenius above *T_g*. Nakamura^{20,28,30} concluded that the ion pair motion (associated with ion pairs exchanging their counteranions with neighboring ion pairs) is strongly correlated with ionic conductivity. From comparison between dielectric and viscoelastic spectra, these authors also show that dielectric ion pair motion is faster than viscoelastic segmental motion. This is opposite to that observed in other ionomers^{29,31,32} (that have lower ion content than the PIL studied in ref 20), where the ion pair motion is ~100× slower than the segmental motion.

Previously, we conducted an extensive investigation of the effect of imidazolium pendant structures, particularly tail type²¹ (*N*-*n*-butyl vs *N*-diethyleneoxy) and length²⁹ (*N*-*n*-butyl vs *N*-*n*-dodecyl), on ion migration, aggregation, dielectric constant, and polymer chain dynamics. The introduction of diethyleneoxy into the imidazolium cation (instead of *n*-butyl) affected the thermal and ion transport properties of the PILs: the *N*-substituent diethyleneoxy imparted higher ion mobility than the *N*-substituent *n*-butyl, for both monomers and polymers, by promoting ion dissociation and lowering *T_g*. In addition, *n*-dodecyl tails resulted in strong ion aggregation, as clearly seen in X-ray scattering, whereas the *n*-butyl tails promoted very little ionic aggregation, resulting in a significantly larger dielectric constant, imparting higher mobilities for the simultaneously conducting ions.²⁹

Herein, we explore the dielectric and viscoelastic response of imidazolium-based PILs with different counterions and side

chain lengths. The glass transition temperatures (*T_g*), storage (*G'*) and loss (*G''*) moduli, ionic conductivities (*σ_{DC}*), and dielectric constants (*ε_s*) of these ionomers are reported. The viscoelastic and dielectric measurements are particularly powerful tools for investigating the impact of associating ion pairs or aggregates as well as the motion of molecules or substituent groups over a broad time range.^{33,34} Electrode polarization (EP) at lower frequencies in dielectric measurements can also be interpreted to estimate the number density of simultaneously conducting ions and their mobilities.^{35–37} EP analysis has recently been utilized with great success for many single-ion conductors above *T_g*.^{21,29,31,38,39} Our studies of polymer dynamics are complemented by morphology studies using X-ray scattering.

EXPERIMENTAL SECTION

Figure 1 shows the molecular structures of the imidazolium methacrylate polymers with (a) an intermediate side chain length and Tf₂N[−] counterions (referred to as Intermediate-Tf₂N), (b) intermediate side chain length and BF₄[−] (referred to as Intermediate-BF₄), and an imidazolium acrylate with (c) a longer side chain length and Tf₂N[−] (referred to as Long-Tf₂N). The findings on these PILs are also compared with those from an earlier study²⁰ of an imidazolium acrylate polymer with (d) a shorter side chain and Tf₂N[−] (referred to as Short-Tf₂N). The dielectric and mechanical responses of acrylate and methacrylate polymers are known to be insensitive to the rigidity of the main chain,⁴⁰ while there is a pronounced dependence of the structure and dynamics on the side chain length.^{41–44} The ionomers were synthesized as described earlier^{26,29} (for the Intermediate ionomers see ref 26 and the Long ionomer see ref 29).

Thermal Characterization. Glass transition temperatures (*T_g*) were determined using a TA Instruments Q100 differential scanning calorimeter (DSC) using 10 K/min cooling and heating rates on ~10 mg samples. *T_g* is taken as the midpoint of the heat capacity change in the second heating.

Linear Viscoelasticity (LVE). Linear viscoelastic response of the imidazolium-based ionomers was studied in oscillatory shear using a Rheometric Scientific Advanced Rheometric Expansion System (ARES)-LS1 rheometer with a force rebalance transducer measuring 0.2–2000 g·cm torque. All samples were dried under vacuum at 80 °C for 72 h to remove voids and water and then loaded to parallel plates with diameter of either 7.9 mm at temperature more than 30 K above *T_g* or 3.1 mm at temperatures near *T_g*. Each sample was then annealed in the instrument at 120 °C in a heated stream of nitrogen for 2 h prior to measurements, for precise geometry and proper contact (wetting of the aluminum plates) and removal of water. At each temperature studied the storage and loss moduli were measured in a

frequency range of 10^{-2} – 10^2 rad/s and at small strain amplitudes (linear response).

Dielectric Relaxation Spectroscopy (DRS). The dielectric measurements of the ionomers were performed using dielectric relaxation spectroscopy. Samples were prepared for the measurement by allowing them to flow to cover a 30 mm diameter freshly polished brass electrode at 100 °C *in vacuo*. To control sample thickness, either Teflon spacers with 200–500 μm heights for Intermediate- BF_4^- and - TF_2N^- , or a silica spacer 50 μm high for Long- TF_2N^- (due to limited sample quantity), were placed on top of the appropriate sample after it flowed to cover the electrode. Then a 20 mm diameter freshly polished brass electrode was placed on top to form a parallel plate capacitor cell which was squeezed to a gap controlled by the spacer in the instrument (with precise thickness checked after dielectric measurement was complete). The ionomer/electrode sandwiches were positioned in a Novocontrol GmbH Concept 40 broadband dielectric spectrometer, after being in a vacuum oven at 100 °C for 24 h. Each sample was then annealed in the instrument at 120 °C in a heated stream of nitrogen for 1 h prior to measurement to remove moisture acquired during sample loading. The dielectric permittivity was measured using a sinusoidal voltage with amplitude 0.1 V over a 10^{-2} – 10^7 Hz frequency range in all experiments. Data were collected in isothermal frequency sweeps every 5 K, from 120 °C to below T_g .

X-ray Scattering. X-ray scattering was performed with a multiangle system that generates Cu K α X-rays, $\lambda = 0.154$ nm, from a Nonius FR 591 rotating anode operated at 40 kV and 85 mA. The bright, highly collimated beam was obtained via Osmic Max-Flux optics and pinhole collimation under vacuum. The scattering data were collected using a Bruker Hi-Star two-dimensional detector with a sample-to-detector distance of 11 cm. To minimize the exposure of the materials to moisture, previously dried samples were inserted into 1 mm glass capillaries and dried under vacuum at 110 °C. As the samples flowed into the capillary under vacuum, bubbles were eliminated. The filled capillaries were cooled to room temperature under vacuum and sealed. The X-ray scattering profiles were evaluated using Datasqueeze software.⁴⁵ The experimental intensities were first corrected for primary beam intensity and background scattering from an empty 1 mm glass capillary was subtracted. Intensities were not corrected for sample density. The isotropic 2-D scattering patterns were azimuthally integrated to yield intensity versus scattering wavevector.

RESULTS AND DISCUSSION

A. Glass Transition Temperature. The imidazolium-based ionomers have a single glass transition, as reported in Table 1. The ionomers do not display crystallization or melting in the temperature range of –80 °C to 200 °C, with 10 K/min heating/cooling rates.

For the Intermediate-ionomers, replacing BF_4^- with TF_2N^- lowered T_g by ~ 70 K, consistent with TF_2N^- counterion acting

Table 1. DSC and LVE Glass Transition Temperatures T_g , Total Ion Concentrations p_0 , Refractive Indices n , and Mass Densities ρ of Ionomers

sample	DSC T_g (K)	LVE ^a T_g (K)	p_0^b (nm ⁻³)	n^b	ρ^b (g/cm ³)
Short- TF_2N	329 ^c		1.95	1.43	1.37
Intermediate- BF_4	358	341	2.20	1.43	1.24
Intermediate- TF_2N	288	276	1.60	1.44	1.33
Long- TF_2N	230	223	1.03	1.46	1.22

^a T_g determined from LVE measurements (defined at $\omega_0(T_g) = 10^{-2}$ rad/s, where ω_0 is the frequency at which the loss modulus (G'') has a maximum in the glassy region, indicating the segmental relaxation time obtained from viscoelastic measurements). ^bTotal ion concentration p_0 , refractive index n , and mass density ρ were determined from a group contribution method based on molecular structure.⁴⁶ ^cValue from ref 20.

as a plasticizer for imidazolium ionic liquids^{14,47} and their polymers.^{10,19,21} Since association of ion pairs allows them to act as temporary cross-links that raise T_g , the more strongly associating BF_4^- imparts higher T_g than TF_2N^- for the imidazolium-based ionomers. This is consistent with the higher quadrupole energy (and slightly larger ratio $E_{\text{quad}}/2E_{\text{pair}}$) for BF_4^- than for TF_2N^- from the *ab initio* calculations in the gas phase (Table 2), indicating that imidazolium- BF_4^- should aggregate more than imidazolium- TF_2N^- . Side chain length also affects the T_g for ionomers with TF_2N^- counterions: T_g decreases as side chain length increases³² [Short- TF_2N ($T_g = 329$ K)^{20,23} > Intermediate- TF_2N ($T_g = 288$ K) > Long- TF_2N ($T_g = 230$ K)]. The T_g s of the four PILs of this study are shown as filled symbols in Figure 2, where they are compared with literature values as open symbols.³² The simple correlation with repeat unit molecular volume^{48,49} V_m in Figure 2 would likely fail if the aggregation factors in Table 2 were significantly different.

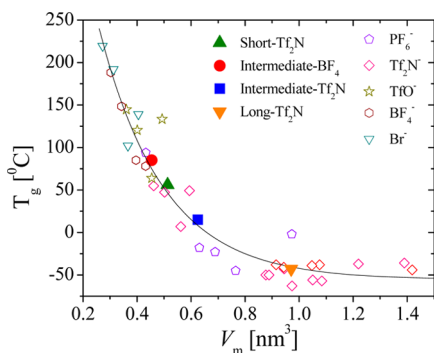
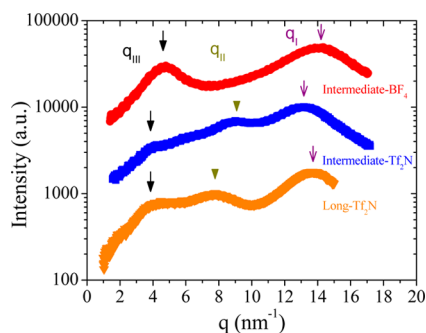
B. X-ray Scattering. Figure 3 compares the room temperature X-ray scattering profiles for the three ionomers with different side chain lengths and counterions. Three distinct peaks are observed: the higher-angle peak at $q_I \approx 14$ nm⁻¹ corresponds to the amorphous halo, the more subtle intermediate-angle peak at $q_{II} \approx 9$ nm⁻¹ has been attributed to correlation between the anions,^{27,51–53} and the lower-angle peaks at $q_{III} \approx 4$ nm⁻¹ for the TF_2N^- ionomers and $q_{III} \approx 5$ nm⁻¹ for the BF_4^- ionomer indicate the spacing between ion aggregates.^{29,54}

For the amorphous halos at q_I of the Intermediate-ionomers, the peak shifts to slightly lower wavevector as the anion size increases from BF_4^- to TF_2N^- . A similar shift is also observed for the anion–anion scattering peak at q_{II} of the TF_2N^- ionomers as the side chain length increases. However, the BF_4^- ionomer does not display a scattering peak at q_{II} . This presumably indicates that due to similarities in electron density of the polymer backbone, side chains, and counterions, the X-ray scattering contrast is low.^{27,55} In contrast, the scattering peak at q_{III} due to ionic aggregation shifts to higher q and its intensity increases significantly as the anion size decreases from TF_2N^- to BF_4^- . The increase in the ionomer peak (q_{III}) intensity suggests that the ionomer with the BF_4^- counterion has more extensive ion aggregation than the TF_2N^- ionomers because the ionomer peak (q_{III}) intensity arises from both the uniformity of the interaggregate spacing and the electron density difference between the matrix and the ionic aggregates.⁵⁶ The reduction in ionic aggregates for large anions is also reflected in the T_g values reported in Table 1 and Figure 2.

C. Linear Viscoelastic Response. To verify the effect of side chain length and counterion type on T_g and ionic aggregation in these ionomers, we study their viscoelasticity, which allows observation of the impact of associating ion pairs or aggregates acting as physical cross-links between chains.^{57–68} Figure 4 shows the master curves of the storage $b_T G'$ and loss $b_T G''$ moduli on frequency $a_T \omega$ for these ionomers, constructed using time–temperature superposition (tTS) referenced at the LVE T_g (defined and listed in Table 1) + 12 K and using frequency- and modulus-scale multiplicative shift factors a_T and b_T , respectively. tTS works well for these materials, consistent with an earlier finding of the success of tTS for imidazolium-based ionomers with various counteranions.^{22,28} Long- TF_2N with $M_w = 15\,800$ g/mol²¹ exhibits terminal liquid response,⁶⁹ with low-frequency limits of $G' \sim \omega^2$ and $G'' \sim \omega$. However,

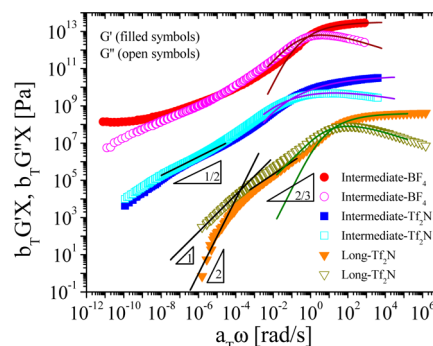
Table 2. *Ab Initio* Interaction Energies^a at 0 K in the Gas Phase for Butylmethylimidazolium with BF₄[−] and Tf₂N[−]

counteranion	ion pair E_{pair} (kJ/mol)	triple (+) $E_{\text{tr}+}$ (kJ/mol)	triple (−) $E_{\text{tr}−}$ (kJ/mol)	quadrupole E_{quad} (kJ/mol)	aggregation factor ⁵⁰ $E_{\text{quad}}/2E_{\text{pair}}$	pair dipole m_{pair} (D)
BF ₄ [−]	361	474	470	804	1.11	13.1
Tf ₂ N [−]	310	413	415	680	1.10	14.1

^aAll calculations were performed using density functional theory methods with the Gaussian 03 software package.^{29,50}**Figure 2.** Correlation between DSC glass transition temperature T_g and repeat unit molecular volume⁴⁹ V_m (including the anion) for these four PILs (filled symbols), compared with literature values³² for imidazolium-based PILs with various side chains and counterions (open symbols). T_g s for the four PILs well follow the solid curve, which is a fit to guide the eye, using an exponential curve,³² with the large V_m limit having $T_g = -52$ °C.**Figure 3.** X-ray scattering intensity as a function of scattering wavevector q for the imidazolium-based ionomers at room temperature. The arrows indicate peaks that correspond to the amorphous halo (q_{II}), anion–anion correlations (q_{III}), and separation between ionic aggregates (q_{III}). The relative ionomer peak (q_{III}) intensity increases as the anion size decreases from Tf₂N[−] to BF₄[−], which we interpret to signify that small counterions favor ion aggregation, consistent with $\sim 15\%$ higher energies for BF₄[−] compared to Tf₂N[−] in Table 2. The data were shifted on the log intensity scale for clarity.

Intermediate-Tf₂N did not reach terminal response at frequencies nearly 5 orders of magnitude lower than Long-Tf₂N (corresponding to 0.01 rad/s at the highest $T = 200$ °C).

For Intermediate-BF₄ with $M_w = 61\,100$ g/mol,²⁶ while the LVE $T_g = 68$ °C, the terminal response reached at temperatures up to 200 °C is that of a cross-linked network at the lowest frequency with modulus of 1400 Pa. This small modulus level is challenging to understand, as it is far smaller than kT per ion, kT per ionic aggregate, or even kT per chain. Since Intermediate-Tf₂N with $M_w = 43\,100$ g/mol²⁶ does not exhibit any plateau, the plateau in Intermediate-BF₄ is attributed to the strong ionic associations that occur in the ionomer with small BF₄[−] counterions, also reflected in the higher T_g (Table 1) and the stronger q_{III} peak in the intensity of X-ray scattering (Figure

**Figure 4.** Storage ($b_T G'$, filled symbols) and loss ($b_T G''$, open symbols) moduli for imidazolium-based ionomers with BF₄[−] or Tf₂N[−] counterions. Master curves referenced to LVE $T_g + 12$ K: 353 K (Intermediate-BF₄), 288 K (Intermediate-Tf₂N), and 235 K (Long-Tf₂N) are then multiplied by vertical shift factor, X [Intermediate-BF₄ ($X = 10^5$); Intermediate-Tf₂N ($X = 10^2$); Long-Tf₂N ($X = 1$)], for clarity. The solid curves correspond to fits of the high-frequency glassy parts of the master curves to the KWW eq 1.

3). These findings that terminal relaxation time increases with increasing ion content (or decreasing side chain length) and decreasing counterion size have been observed in other ionomers.^{63–65,70} The slope of the glass-to-rubber transition region ($10^{-8} < a_T \omega < 10^{-4}$ rad/s) of G' and G'' versus ω for Intermediate-Tf₂N is $\sim 1/2$, which agrees with the Rouse model,⁶⁹ while the slope of $\sim 2/3$ for Long-Tf₂N in the transition region ($10^{-4} < a_T \omega < 10^{-1}$ rad/s) is akin to the Zimm model⁶⁹ and similar to many conventional polymers, including poly(methyl methacrylate) (PMMA). Furthermore, the glassy part of these master curves at high frequency ($10^{-1} < a_T \omega < 10^6$ rad/s) is well described by the empirical Kohlrausch–Williams–Watts (KWW) model, which appears to fit data well for various glass-formers (see solid curves in Figure 4):^{34,71}

$$G_g(t) = G_g(0) \exp[-(t/\tau_{\text{KWW}})^\beta] \quad (1)$$

wherein $G_g(t)$ is the stress relaxation modulus, $G_g(0)$ is the glassy modulus, τ_{KWW} is a characteristic time of the glassy relaxation, and β is the stretching exponent to specify the glassy relaxation mode distribution (i.e., lower β value indicates a broader mode distribution).⁷² In Figure 4, Intermediate-Tf₂N ($\beta \sim 0.2$) has a broader mode distribution than either Long-Tf₂N ($\beta \sim 0.35$) or Intermediate-BF₄ ($\beta \sim 0.35$). This broadening is also observed in DSC, with a significantly broader transition in Intermediate-Tf₂N than in Intermediate-BF₄ and Long-Tf₂N (see Supporting Information, Figure S1), but is not understood.

The temperature dependence of the frequency-scale shift factors, a_T , used to construct Figure 4 obeyed the Williams–Landel–Ferry (WLF) equation⁷³ (see Figure 5):

$$\log a_T = -\frac{c_1(T - T_r)}{c_2 + T - T_r} = -\frac{c_1(T - T_r)}{T - T_0} \quad (2)$$

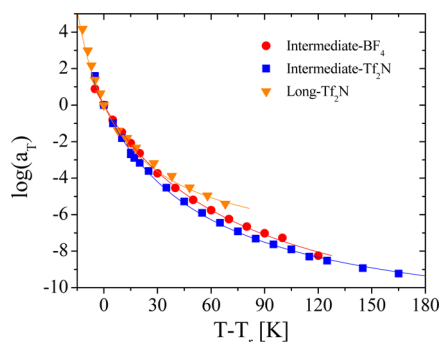


Figure 5. Temperature dependence of shift factors a_T for time-temperature superposition of oscillatory shear data vs $T - T_r$ ($T_r = \text{LVE } T_g + 12 \text{ K}$). The solid curves are fits to the WLF equation (eq 2).

wherein c_1 and $c_2 = T_r - T_0$ are constants, $T_r = \text{LVE } T_g + 12 \text{ K}$ is the reference temperature, and T_0 is the Vogel temperature. The fit parameters c_1 , c_2 , and T_0 are given in Table 3. The fact that c_1 and c_2 increase with increasing ion content (or decreasing side chain length) is similar to what was found by Weiss et al.⁷⁰ for sulfonated polystyrene ionomers and indicates that the fractional free volume near T_g decreases due to strong intermolecular associations, moving T_g to a higher temperature.⁷⁴ The Vogel temperature T_0 is typically $\sim 50 \text{ K}$ below T_g for polymers and correlated with $D \cong 2.303c_1c_2/T_0$; Table 3 shows $(T_g - T_0)/D \cong 7 \text{ K}$ for all three ionomers.

D. Ionic Conductivity. Figure 6 displays the temperature dependence of DC conductivity, evaluated from a roughly 3 decade frequency range where the in-phase part of the conductivity $\sigma'(\omega) = \epsilon''(\omega)\epsilon_0\omega$ is independent of frequency, as shown in Figure 7. There is a significant influence of counterion type on ionic conductivity for ionomers. Because of the suppression of T_g , the larger Tf_2N^- anion increases ionic conductivity of Intermediate- Tf_2N by $\sim 1000\times$ at room temperature compared to Intermediate- BF_4 . However, the 30°C conductivities of the corresponding neat ILs are similar: 4.6 mS/cm for butylmethylimidazolium with BF_4^- and 4.5 mS/cm for that with Tf_2N^- .⁷⁵ For Short- Tf_2N and Intermediate- Tf_2N and - BF_4 , we observe a change in character near T_g where the temperature dependence of ionic conductivity changes from a Vogel–Fulcher–Tammann (VFT) form ($T > T_g$) to an Arrhenius form ($T < T_g$).

This abrupt change in the temperature dependence of the conductivity has also been found at the glass transition temperature of inorganic glassy electrolytes.⁷⁹ However, the temperature dependence of the conductivity for Long- Tf_2N simply follows a VFT dependence because the DC conductivity below T_g is far too low to be measurable in DRS. Previous computer simulations indicated that for nonpolymeric imidazolium ILs the distribution of the charged domains (anion/cation pairs) is not homogeneous, but instead consists of a continuous 3D network of ionic domains, coexisting with nonpolar (alkyl chain) domains which form dispersed micro-

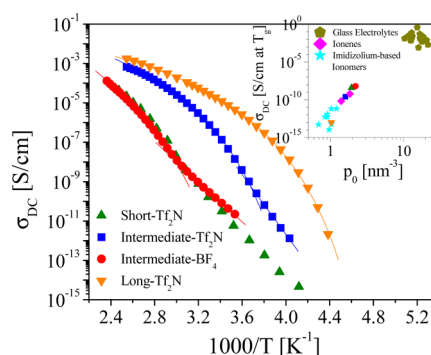


Figure 6. Temperature dependence of ionic conductivity for Tf_2N^- and BF_4^- ionomers, including literature data from ref 20 for Short- Tf_2N (green triangles). Lines indicate fits to eq 16. The inset indicates the DC conductivity at T_g as a function of total ion content p_0 . For comparison, σ_{DC} at T_g for inorganic glass electrolytes,⁷⁶ ionenes,^{77,78} and other imidazolium-based ionomers^{29,32} are also included.

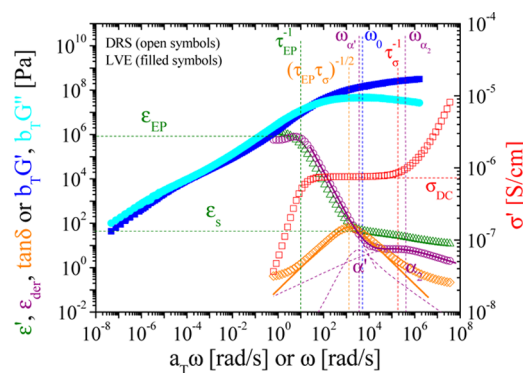


Figure 7. Dielectric and viscoelastic spectra for Intermediate- Tf_2N at 303 K . The dielectric derivative $\epsilon'_{\text{der}} = -\pi/2 \times \partial \epsilon''(\omega)/\partial \ln \omega$ (purple open circles) shows two dielectric relaxations (purple dashed curves) designated as α' at $\omega_{\alpha'}$ and α_2 at ω_{α_2} , and the purple solid line indicates the result from analyzing ϵ'_{der} with one power law⁸⁴ plus two Havriliak–Negami (HN) functions. After ion motion becomes diffusive at τ_{σ} the in-phase part of the conductivity σ' (red open squares) levels to σ_{DC} and the static dielectric constant ϵ_s in the dielectric permittivity ϵ' (green open triangles) is enhanced by orientational polarizations (α' and α_2).³² At low frequencies EP is complete on the electrode polarization time scale τ_{EP} , and the permittivity significantly increases to ϵ_{EP} . The peak of the loss tangent $\tan \delta$ (orange open diamonds) gives the geometric mean of the time scales of electrode polarization and conductivity $(\tau_{\text{EP}}\tau_{\sigma})^{1/2}$, evaluated from eq 5 (orange solid line). Master curves of storage ($b_T G'$, blue solid squares) and loss ($b_T G''$, cyan solid circles) moduli for Intermediate- Tf_2N at the reference temperature of 303 K are also included. The relaxation time of the monomer ($\tau_0 = 1/\omega_0$), evaluated as the reciprocal of the frequency at which the loss modulus has a maximum in the glassy region, indicates the segmental relaxation time obtained from viscoelastic measurements and agrees well with $1/\omega_{\alpha'}$.

Table 3. Temperature Dependence of the LVE Shift Factors Fit to the WLF Equation (Eq 2), with $T_r = \text{LVE } T_g + 12 \text{ K}$

sample	c_1	$c_2 \text{ (K)}$	$T_0 \text{ (K)}$	D^a	LVE $T_g - T_0 \text{ (K)}$	(LVE $T_g - T_0$)/ $D \text{ (K)}$
Intermediate- BF_4	13.4	80	273	8.9	68	7.6
Intermediate- Tf_2N	11.5	48	240	5.3	36	6.8
Long- Tf_2N	8.4	39	196	3.9	27	6.9

^aSince the WLF equation (eq 2) is mathematically equivalent to the VFT equation (eq 14), $D \cong 2.303c_1c_2/T_0$.

phases.^{80,81} When the PILs have short side chains (high ion content) the ion domains are presumably continuous, thereby raising the conductivity and allowing measurement far below T_g with Arrhenius character, as seen for inorganic glasses. This is also reflected in the inset of Figure 6, which shows that the DC conductivity at T_g increases with total ion content p_0 for various single-ion conductors.^{29,32,76–78} To further understand the conduction mechanism, we analyze electrode polarization to investigate the temperature dependence of the number density of simultaneously conducting ions p and their mobility μ .

E. Electrode Polarization Analysis. A physical model of electrode polarization (EP) allows separation of ionic conductivity into the number density of simultaneously conducting ions and their mobility,^{35–37,82,83} as has recently been done for other single-ion conductors above T_g .^{29,31,38,39} Electrode polarization occurs at low frequencies, where the transporting ions have sufficient time to polarize at the blocking electrodes during the cycle. That polarization manifests itself in (1) an increase in the effective capacitance of the cell (increasing the dielectric constant ϵ' ; see Figure 7) and (2) a decrease in the in-phase part of the conductivity σ' , as the polarizing ions reduce the field experienced by the transporting ions. The time scale for conduction is the time where counterion motion becomes diffusive

$$\tau_\sigma \equiv \frac{\epsilon_s \epsilon_0}{\sigma_{DC}} \quad (3)$$

wherein ϵ_s is the measured static relative permittivity of the sample before EP and ϵ_0 is the permittivity of vacuum. At low frequencies the conducting ions start to polarize at the electrodes and fully polarize at the electrode polarization time scale

$$\tau_{EP} \equiv \frac{\epsilon_{EP} \epsilon_0}{\sigma_{DC}} \quad (4)$$

wherein ϵ_{EP} is the (considerably larger) effective permittivity after electrode polarization is complete (see Figure 7 and Supporting Information Figure S2). The Macdonald and Coelho model^{35–38,83} treats electrode polarization as a simple Debye relaxation with loss tangent

$$\tan \delta = \frac{\omega \tau_{EP}}{1 + \omega^2 \tau_\sigma \tau_{EP}} \quad (5)$$

In practice, the loss tangent shown in Figure 7 as orange open diamonds is fit to eq 5 to determine the electrode polarization time τ_{EP} and the conductivity time τ_σ . The Macdonald and Coelho model then permits determining the number density of simultaneously conducting ions p and their mobility μ from τ_{EP} and τ_σ

$$p = \frac{1}{\pi l_B L^2} \left(\frac{\tau_{EP}}{\tau_\sigma} \right)^2 \quad (6)$$

$$\mu = \frac{e L^2 \tau_\sigma}{4 \tau_{EP}^2 k T} \quad (7)$$

wherein $l_B \equiv e^2 / (4 \pi \epsilon_s \epsilon_0 k T)$ is the Bjerrum length, L is the spacing between electrodes, k is the Boltzmann constant, and T is absolute temperature.

Conducting Ion Content. The temperature dependence of the number density of simultaneously conducting ions p calculated from eq 6 is plotted in Figure 8, and the fraction of

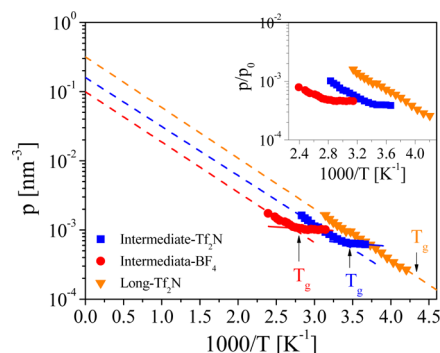


Figure 8. Temperature dependence of simultaneously conducting ion concentration p . Dashed (above T_g) and solid (below T_g) lines are Arrhenius fits to eq 8 with two fitting parameters (E_a^p and p_∞ , listed in Table 4). T_g is indicated by arrows; for Long- Tf_2N , p was measurable only at temperatures above T_g . The inset displays the fraction of anions simultaneously participating in conduction (p divided by the total anion concentration p_0).

ions participating in conduction (p/p_0 where p_0 , listed in Table 1, is the total anion number density) is shown in the Figure 8 inset. The temperature dependence of simultaneously conducting ion concentration for these imidazolium-based ionomers above T_g is well described by an Arrhenius equation

$$p = p_\infty \exp \left(- \frac{E_a^p}{RT} \right) \quad (8)$$

wherein p_∞ and E_a^p , listed in Table 4, are the conducting ion concentration as $T \rightarrow \infty$ and the activation energy for conducting ions, respectively. The fact that p_∞ is smaller than p_0 indicates some of the counterions are too strongly aggregated to participate in ionic conduction, and $1 - p_\infty/p_0$ (listed in Table 4) estimates the fraction of counterions that are trapped in local environments.^{29,85,86} Not only does the BF_4^- ionomer have more trapped ions than the Tf_2N^- ionomers, but also the Intermediate-ionomers have many more trapped ions than the Long-ionomer. This suggests that smaller counterion and shorter side chain lead to stronger ionic aggregation, consistent with the viscoelastic measurements in section C and the analysis of the static dielectric constant in section F.

It is evident that Intermediate- BF_4 and - Tf_2N show a transition in conducting ion concentration at T_g . In other words, both ionomers have two p_∞ s and E_a^p s, listed in Table 4, one set above and the other below T_g . The values of p_∞ below T_g are much lower than those above T_g , suggesting that only $\sim 0.1\%$ ($p_\infty/p_0 \sim 0.001$) are not trapped below T_g . The fact that below T_g the Long-ionomer has lower p than the Intermediate-ionomers indicates that its trapped ion fraction may be even higher than $\sim 99.9\%$ below T_g . To explain the results, we propose a simple model for the conducting mechanism at temperatures above vs below T_g . Above T_g , the dominant conducting species is the negative triple ion that moves by segmental motion, whereas below T_g the segmental motion ceases and only the very tiny population of free anions can conduct. This is presumably why the Intermediate-ionomers show lower p_∞ and E_a^p below T_g than above T_g in Table 4.

The inset in Figure 8 shows that the fraction of counterions simultaneously participating in conduction in these single-ion conductors is quite low, $<0.1\%$ of the total counterions. The conducting ion content evaluated from the EP model is the number density of ions in a conducting state in any snapshot,

Table 4. Fitting Parameters of the Arrhenius Equation for Conducting Ion Content, Eq 8, and the VFT ($T > T_g$) and Arrhenius ($T < T_g$) Equations for Conducting Ion Mobility, Eq 9

sample	conducting ion content						conducting ion mobility				
	$T > T_g$			$T < T_g$			$T > T_g$		$T < T_g$		
	p_0 (nm ⁻³)	p_∞ (nm ⁻³)	E_a^p (kJ/mol)	$1 - p_\infty/p_0$	p_∞ (nm ⁻³)	E_a^p (kJ/mol)	μ_∞ (cm ² V ⁻¹ s ⁻¹)	D	T_0 (K)	μ_∞ (cm ² V ⁻¹ s ⁻¹)	E_a^μ (kJ/mol)
Intermediate-BF ₄	2.20	0.09	13.9	0.96	0.002	1.3	12.59	8.9	228	7.9×10^7	96
Intermediate-Tf ₂ N	1.60	0.16	13.4	0.90	0.001	1.7	0.63	4.5	218	2.5×10^{19}	144
Long-Tf ₂ N	1.03	0.33	14.1	0.68	<i>a</i>	<i>a</i>	0.08	3.4	196	<i>a</i>	<i>a</i>

^aLong-Tf₂N only has measurable conducting ion content and mobility above T_g .

which sets the boundary condition for the solution of the Poisson–Boltzmann equation. For this reason, only a small fraction of total ions are in a conducting state at any given instant in time, similar to observations on other single-ion conducting ionomers with alkali metal counterions^{31,38,39} or ionic liquid counterions.^{21,29,65,85}

Mobility of Conducting Ions. The temperature dependence of the mobility of the simultaneously conducting ions determined from the EP model is displayed in Figure 9 as

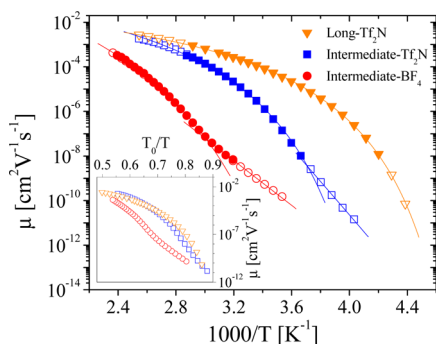


Figure 9. (a) Temperature dependence of the mobility of the simultaneously conducting ions, determined from (1) the EP model (filled symbols) and (2) dividing the DC conductivity data by the product of the elementary charge e and the Arrhenius fit to eq 8 of simultaneously conducting ion number density p (open symbols, referred to as extended mobility). Both mobility and extended mobility above and below T_g are fit to eq 9 as solid lines. The inset exhibits the ionic mobilities with respect to inverse temperature normalized by T_0 .

the filled symbols. Since conductivity can be measured over a far wider temperature range, we divide the DC conductivity data in Figure 6 by the elementary charge e and by the Arrhenius fits to eq 8 of simultaneously conducting ion number density p (with E_a^p and p_∞ above and below T_g in Table 4) to determine an extended range of mobility, plotted in Figure 9 as the open symbols.²⁹ Mobility and extended mobility are then collectively fit to the VFT equation above T_g and the Arrhenius equation below T_g :

$$\mu = \mu_\infty \exp\left(-\frac{DT_0}{T - T_0}\right) \quad \text{for } T > T_g$$

$$\mu = \mu_\infty \exp\left(-\frac{E_a^\mu}{RT}\right) \quad \text{for } T < T_g \quad (9)$$

wherein μ_∞ is the high-temperature limit of the mobility, T_0 is the Vogel temperature, and D is the so-called strength parameter (reciprocally related to fragility); those fitting

parameters are found in Table 4. The ion mobility of the Tf₂N[−] ionomers is higher than that of the BF₄[−] ionomer because the larger Tf₂N[−] anion imparts lower T_g . The lower T_g also explains the higher mobility of the ionomer with longer side chains than with shorter side chains. Furthermore, the effect of the counterion on ion mobility is clearly observed from the mobilities plotted against T_0/T (see inset of Figure 9), which accounts for the difference in Vogel temperature T_0 among the ionomers. The data do not merge into a single curve, but instead yield two separate curves. The ionomers with the larger Tf₂N[−] have higher mobility and higher fragility (lower D) than that with the smaller BF₄[−] for the same T_0/T because imidazolium binds Tf₂N[−] weaker than BF₄[−] (see Table 2). This trend reverses in the glass, where the Arrhenius temperature dependence of ion mobility below T_g exhibits higher activation energy for ion mobility of the Tf₂N[−] ionomer than the BF₄[−] ionomer (see Table 4), presumably because with limited segmental motion the larger Tf₂N[−] has a higher potential barrier in the glassy state, where free volume limits counterion motion.

F. Static Dielectric Constant. Figure 10 displays the frequency dependence of the dielectric permittivity $\epsilon'(\omega)$ for

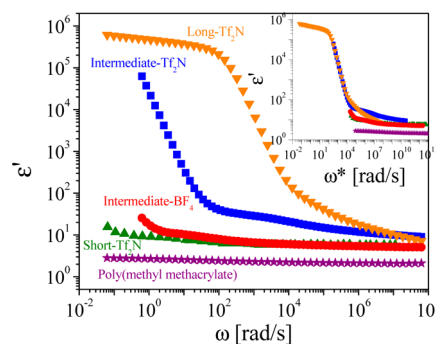


Figure 10. Frequency dependence of dielectric permittivity ϵ' for imidazolium-based ionomers and nonionic poly(methyl methacrylate) at $T = 283$ K, including literature data from ref 20 for Short-Tf₂N (green triangles). The inset shows ϵ' shifted horizontally to compare the static dielectric constant, usually defined as the value of ϵ' just above the frequency at which electrode polarization commences (see Figure 7).

these ionomers and nonionic poly(methyl methacrylate) (PMMA) at 283 K. The static dielectric constant ϵ_s is defined as the low frequency plateau of $\epsilon'(\omega)$ before the onset of EP.^{29,31,32,38,65,85}

However, except for nonionic PMMA, $\epsilon'(\omega)$ was not observed to clearly plateau before EP, but to gradually decrease with increasing frequency, indicating underlying relaxations, as

seen in all ionomers with reasonable conductivity.^{29,31,32,38,39,56,65,85} To display the ϵ_s difference with side chain length, the dielectric constant spectra in the inset of Figure 10 were horizontally shifted to superimpose EP. The ionomers with longer side chains exhibit higher ϵ_s than those with shorter side chains, and all ionomers have much higher ϵ_s than the nonionic PMMA. There are two reasons for the lower ϵ_s for ionomers with shorter side chains as (1) they necessarily have higher ion content that encourages ion aggregation and (2) they have very restricted motion of the imidazolium cations due to the proximity of the ionomer backbone.³² Combining the imidazolium cations with longer nonionic segments allows ions to more readily respond to the field.

Figure 11 displays the temperature dependence of the static dielectric constant, calculated using eq 3 from the measured

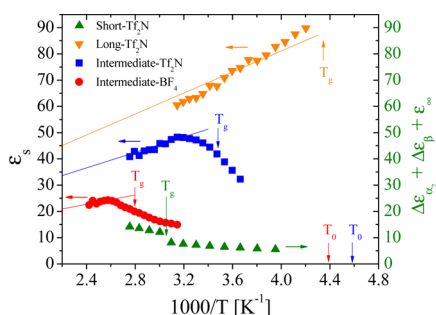


Figure 11. | Temperature dependence of static dielectric constant ϵ_s for Intermediate- and Long-Tf₂N, including literature data ($\epsilon_s \approx \Delta\epsilon_{\alpha_2} + \Delta\epsilon_{\beta} + \epsilon_{\infty}$) from ref 20 for Short-Tf₂N. The solid lines are thermal randomization fits of data in temperatures above $T_g + 30$ K (for Intermediate-ionomers) and over the whole temperature range studied (for Long-Tf₂N) to the Onsager equation (eq 10) with fixed concentration and strength of dipoles. T_g and T_0 are indicated by arrows.

σ_{DC} and τ_{σ} obtained from fitting EP to eq 5.^{29,38,65,85} The temperature dependence of ϵ_s for Long-Tf₂N follows the Onsager equation^{29,87,88} across the entire temperature range

$$\frac{(\epsilon_s - \epsilon_{\infty})(2\epsilon_s + \epsilon_{\infty})}{\epsilon_s(\epsilon_{\infty} + 2)^2} = \frac{1}{9\epsilon_0 kT} \sum_i \nu_i m_i^2 \quad (10)$$

where ν_i is the number density of dipoles, m_i is their dipole moment, and ϵ_{∞} is the high-frequency limit of the dielectric constant (here taken to as $\epsilon_{\infty} = n^2$, where n is the refractive index, estimated from group contributions and listed in Table 1). This indicates that the static dielectric constant decreases as temperature increases (as $1/T$) from thermal randomization.

For Intermediate-Tf₂N and -BF₄, ϵ_s first increases with decreasing temperature until about $T_g + 30$ K is reached ($\epsilon_s \sim 1/T$), but then ϵ_s begins to decrease with decreasing temperature. This nonmonotonic temperature dependence is entirely unexpected in Onsager's theory, which is only applicable to the motion of molecules with polar groups in the liquid state at temperatures far above T_g at which their motion is unrestricted by neighbors. As temperature is lowered toward T_g , the molecular motion is expected to be restricted by neighbors, which limits rotation/alignment of dipoles under an applied field, thereby leading to ϵ_s decreasing on cooling near T_g . Such a decrease in ϵ_s near T_g has been observed in nonionic polar polymers (such as poly(alkyl methacrylates)),^{42,43} a vinylidene chloride–vinyl chloride copolymer,^{89–91} and poly-

acetaldehyde⁹²) and in the Short-Tf₂N ionomer.²⁰ There is also a significant effect of anion type on the static dielectric constant of these ionomers. The ionomer with the smaller BF₄[−] exhibits a significantly lower static dielectric constant than those with larger Tf₂N[−], similar to other ionomers.^{65,85} This is due to the fact that BF₄[−] binds more strongly than Tf₂N[−], as anticipated by the *ab initio* calculations presented in Table 2, resulting in more ion aggregation in the BF₄[−] ionomer, directly affecting its static dielectric constant (Figure 11), morphology (Figure 3), and viscoelasticity (Figure 4).

G. Dielectric Relaxations. To investigate polymer chain or ion dynamics of these ionomers, the loss peaks of dipolar relaxation processes are evaluated. However, electrode polarization and conduction can obscure the loss peaks of interest.³⁴ Thus, we use the derivative formalism,⁹³ which eliminates the conductivity contribution from loss spectra, to elucidate relaxation processes:^{31,39}

$$\epsilon_{\text{der}} = -\frac{\pi}{2} \frac{\partial \epsilon'(\omega)}{\partial \ln \omega} \quad (11)$$

The dipolar relaxations were then explored by fitting the derivative spectra with one power law⁸⁴ for EP plus two Havriliak–Negami (HN) functions for two dielectric relaxations (α_2 and either α or α' : see Figure 12)

$$\epsilon_{\text{der}} = A\omega^{-s} - \frac{\pi}{2} \left(\left[\frac{\partial \epsilon'_{\text{HN}}(\omega)}{\partial \ln \omega} \right]_{\alpha_2} + \left[\frac{\partial \epsilon'_{\text{HN}}(\omega)}{\partial \ln \omega} \right]_{\alpha \text{ or } \alpha'} \right)$$

with $\epsilon'_{\text{HN}}(\omega) = \text{Real} \left\{ \frac{\Delta\epsilon}{[1 + (i\omega/\omega_{\text{HN}})^a]^b} \right\}$ (12)

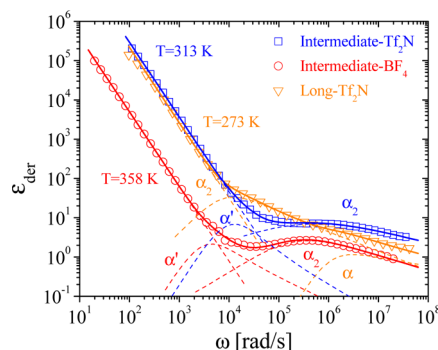


Figure 12. Dielectric derivative spectra fit (solid lines) to the sum of a power law⁸⁴ for EP and derivative forms of the HN function for ion rearrangement (α_2) of these ionomers and either polymer segmental motion of Long-Tf₂N (α) or slowed-down polymer segmental motion of Intermediate-Tf₂N and -BF₄ (α'). Individual contributions of the relaxations are shown as dashed lines.

where A and s are constants ($s = 1.9$), $\Delta\epsilon$ is the relaxation strength, a and b are the shape parameters, and ω_{HN} is a characteristic frequency related to the frequency of maximal loss ω_{max} by^{34,94,95}

$$\omega_{\text{max}} = \omega_{\text{HN}} \left(\sin \frac{a\pi}{2 + 2b} \right)^{1/a} \left(\sin \frac{ab\pi}{2 + 2b} \right)^{-1/a} \quad (13)$$

In the derivative spectra of Figure 12, Long-Tf₂N exhibits two dielectric relaxations designated as α and α_2 , in the order of decreasing frequency, with α_2 stronger than the α process. For Intermediate-Tf₂N and -BF₄ it was not possible to fit the

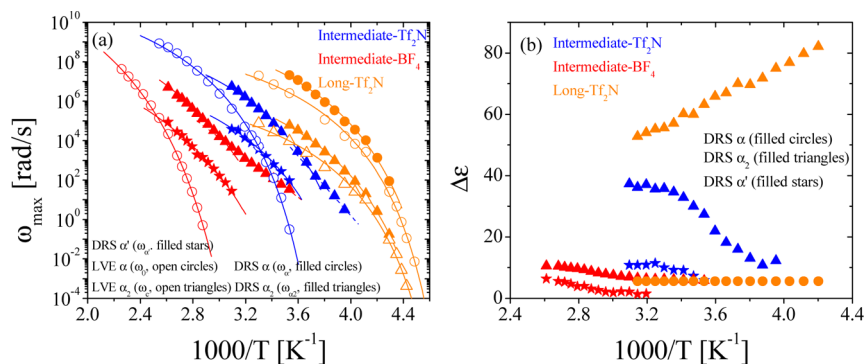


Figure 13. Temperature dependence of (a) relaxation peak frequency ω_{\max} and (b) relaxation strengths $\Delta\epsilon$ of α (filled circles), α_2 (filled triangles), and α' (filled stars) processes from DRS. Solid lines are fits of the VFT equation (eq 14) using T_0 from the VFT fits of mobility in Figure 9, and dashed lines are fits of the Arrhenius equation (eq 15) using E_a^μ from the Arrhenius fits of mobility in Figure 9. Segmental relaxation frequencies ω_0 where loss modulus (G'') has a maximum, corresponding to segmental motion from LVE (open circles), and characteristic frequencies ω_c at which $G'(\omega_c) = p_0kT$, corresponding to ionic dissociation from LVE (open triangles), are also included.

Table 5. Temperature Dependence of the α_2 , α' , and α Processes, Fit to Eq 14 ($T > T_g$) and Eq 15 ($T < T_g$)

sample	dielectric response									viscoelastic response					
	α_2 process ($T > T_g$)			α_2 process ($T < T_g$)			α or α' process ($T > T_g$)			α process ($T > T_g$)			α_2 process ($T > T_g$)		
	T_0 (K)	$\log(\omega_\infty)$ (rad/s)	D	E_a^μ (kJ/mol)	$\log(\omega_\infty)$ (rad/s)	T_0 (K)	$\log(\omega_\infty)$ (rad/s)	D		T_0 (K)	$\log(\omega_\infty)$ (rad/s)	D	T_0 (K)	$\log(\omega_\infty)$ (rad/s)	D
Intermediate-BF ₄	228	12.0	8.2	96	19.2	228	10.2	8.5		273	13.8	8.9	<i>c</i>	<i>c</i>	<i>c</i>
Intermediate-Tf ₂ N	218	10.8	4.6	144	30.2	218	9.0	4.9		240	12.5	5.3	<i>c</i>	<i>c</i>	<i>c</i>
Long-Tf ₂ N	196	8.7	4.1	<i>b</i>	<i>b</i>	196	11.3	4.1		196	10.1	3.7	196	7.7	3.7

^aThe Intermediate-ionomers have such strong α_2 relaxation that the underlying α relaxation is not resolvable and instead these ionomers exhibit weak α' relaxation, owing to their high ion content, while the Long-Tf₂N displays a clear α relaxation, owing to its lower ion content. ^bThe ionomer with the Long side chains only has measurable α_2 relaxation above T_g . ^cThe sticky Rouse model allows estimating ion association time (α_2 process) of the Long-Tf₂N, but not the Intermediate-ionomers.

derivative spectra with a single α_2 relaxation plus a power law; an additional relaxation slower than α_2 (referred to as α') is needed to obtain an acceptable fit. Whether α' is a separate relaxation or simply a pronounced low-frequency broadening of the α_2 relaxation is not clear. Here we adopt the standard interpretation that since the relaxation is too broad to be described by a single HN function, we use two functions for α_2 and α' processes. The peak relaxation frequencies ω_{\max} and relaxation strengths $\Delta\epsilon$ of the α , α' , and α_2 processes are determined from this fitting, and their temperature dependences are displayed in Figure 13. For nonpolymeric ionic liquids, dielectric relaxation processes, originating in the reorientation of the bulky dipolar cation or in mesoscale (larger aggregate or cluster) cooperative motions, are observed.^{96,97} Ionomers show two dipolar relaxations^{29,31,39} assigned to the usual segmental motion of the polymer (α) and a lower frequency relaxation (α_2) attributed to ions rearranging, for example exchanging states between isolated pairs and aggregates of pairs.

The origin of the α' relaxation in Intermediate-ionomers however is not clear. It is presumably related to slowed-down segmental relaxation of polymer segments. The α' peak relaxation frequency ($\omega_{\alpha'}$) is slower than the α_2 peak relaxation frequency (ω_{α_2}) but similar to or faster than the mechanical segmental motion from LVE (ω_0) as shown in Figure 13a. The temperature dependence of the α' relaxation strength ($\Delta\epsilon_{\alpha'}$) is similar to that of the α_2 relaxation strength ($\Delta\epsilon_{\alpha_2}$), but $\Delta\epsilon_{\alpha'}$ is

lower than $\Delta\epsilon_{\alpha_2}$ across the entire temperature range (see Figure 13b).

The peak relaxation frequencies ω_{\max} of the DRS α_2 , α , and α' processes of these ionomers follow VFT (above T_g) or Arrhenius (below T_g) temperature dependence with the same Vogel temperature T_0 or activation energy E_a^μ as were found for the (extended) mobility of simultaneously conducting ions.²⁹

$$\omega_{\max} = \omega_\infty \exp\left(-\frac{DT_0}{T - T_0}\right) \quad \text{for } T > T_g \quad (14)$$

$$\omega_{\max} = \omega_\infty \exp\left(-\frac{E_a^\mu}{RT}\right) \quad \text{for } T < T_g \quad (15)$$

The solid lines for ω_α , ω_{α_2} , and $\omega_{\alpha'}$ in Figure 13a are fits to eq 14 using the T_0 from the VFT fits of mobility in Figure 9 with strength parameter D and high-temperature limiting frequency ω_∞ listed in Table 5. The dashed lines in Figure 13a are fits to eq 15 using the E_a^μ from the Arrhenius fits of mobility in Figure 9 with ω_∞ as the sole fitting parameter. The peak relaxation frequencies of the α_2 , α , and α' processes in these ionomers follow similar temperature dependence as their ionic conductivity (Figure 6) and mobility (Figure 9). For the Intermediate-ionomers, the α_2 peak frequencies and ionic mobilities below T_g display Arrhenius-temperature dependence with the common activation energy (E_a^μ). This reflects the coupling of free ion rearrangement and transport and makes

these ionomers exhibit Arrhenius conductivity at temperatures below T_g .

Figure 13b shows that the relaxation strength $\Delta\epsilon$ for the α_2 process is much larger than those for the α and α' processes, and $\Delta\epsilon_{\alpha_2}$ (triangles) and $\Delta\epsilon_{\alpha'}$ (stars) have the stronger temperature dependence, whereas $\Delta\epsilon_{\alpha}$ (circles) has very weak temperature dependence. This indicates that the stronger α_2 process involving ionic rearrangements primarily determines the temperature dependence of the total ϵ_s shown in Figure 11. The Long-ionomer has much larger $\Delta\epsilon_{\alpha_2}$ than the Intermediate-ionomers, and the BF_4^- ionomer has much lower $\Delta\epsilon_{\alpha_2}$ than the Tf_2N^- ionomers. These differences track perfectly with the total content of ions participating ion conduction (p_∞/p_0). Conversely, a large fraction of aggregated ions ($1 - p_\infty/p_0$, listed in Table 4) hinder motion of the dipoles, leading to a significant decrease of the relaxation strength of the α_2 process, consistent with the small BF_4^- anion promoting ion aggregation, as seen in X-ray scattering (Figure 3).

H. Comparison of Viscoelastic and Dielectric Responses. It is insightful to compare the viscoelastic and dielectric properties. Figure 14 displays the frequency depend-

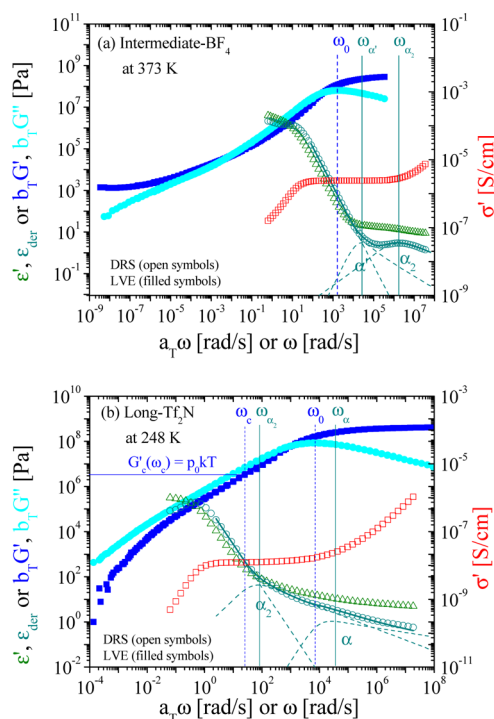


Figure 14. Comparison between viscoelastic and dielectric response of (a) Intermediate- BF_4 (at 373 K) and (b) Long- Tf_2N (at 248 K). The vertical dashed line represents the time scale (ω_0 and ω_c) from viscoelastic measurements, and vertical solid lines represent the time scales (ω_{α_2} , $\omega_{\alpha'}$ and ω_{α}) from dielectric measurements.

ence of viscoelastic master curves (G' and G'') for Intermediate- BF_4 (Figure 14a) and Long- Tf_2N (Figure 14b) at the indicated reference temperatures. For comparison, the frequency dependence of the dielectric spectra (ϵ' , ϵ'' , and σ') are also included. According to the Rouse model,⁶⁹ the relaxation time of the mechanical α process is related to the relaxation time of the monomer or the shortest stress relaxation time τ_0 , corresponding to the reciprocal of the frequency $\tau_0 = 1/\omega_0$ where the loss modulus G'' has a peak in the glassy

region.^{22,28} Like the dielectric α process (ω_{α} filled circles in Figure 13a), the temperature dependence of the LVE α process (ω_0 open circles in Figure 13a) is well described by the VFT equation, eq 14 (solid lines in Figure 13a). In those VFT fits, the resulting D values for DRS α , α_2 , and α' and LVE α relaxations are quite similar for each given ionomer.

Figure 14a shows that the peak frequency of the mechanical segmental motion estimated from LVE measurements (ω_0 indicated by the vertical dashed line) is about 1000 times lower than the relaxation frequency of the dielectric mode at higher frequency (ω_{α_2} indicated by the vertical solid line) but is only 10 times lower than that of the dielectric mode at lower frequency ($\omega_{\alpha'}$ indicated by the vertical solid line) for Intermediate- BF_4 at 100 °C. Intermediate- Tf_2N also shows significantly different ω_0 and ω_{α_2} relaxation frequencies and almost identical ω_0 and $\omega_{\alpha'}$ relaxation frequencies (see Figure 7). Note that such a significantly slower LVE polymer relaxation than DRS ionic (α_2) relaxation has been observed by Nakamura et al.^{22,28,30} for Short- Tf_2N .

In Figure 14b, on the other hand, the ω_0 is close to the dielectric segmental motion (ω_{α} indicated by the vertical solid line), indicating that the fast dielectric mode should originate from the segmental motion of Long- Tf_2N . This similarity of the frequency–temperature position of the α process between the viscoelastic and dielectric measurements has been observed in other polymeric systems.^{98–103} From the sticky Rouse model,^{72,104,105} the chain motion on scales larger than the distance between ionic associations is controlled by the association lifetime τ_s . The time scale corresponding to the sticky Rouse segments can be further evaluated as $\tau_s \sim 1/\omega_c$ where ω_c is the characteristic frequency at which $G'(\omega_c) = p_0 kT$.^{72,105} Figure 14b reveals very close similarity between ω_c and ω_{α_2} for the Long- Tf_2N . This feature is also clearly seen in Figure 13a, where ω_c and ω_{α_2} show the same VFT temperature dependence and nearly identical values across the entire temperature range. This suggests that the chain motion of Long- Tf_2N is governed by the ionic association observed in DRS. Moreover, the ratio of the time scale for motion of polymer segments (τ_a) and the ion association lifetime (τ_{α_2}) can provide a simple estimation of activation energy for an ion pair to dissociate from the cluster as $\tau_{\alpha_2}/\tau_a \cong \exp(E_a/kT)$.⁷² The estimated activation energy is ~ 13 kJ/mol, which is similar as the activation energy for conducting ions ($E_a^p \sim 14$ kJ/mol in Figure 8).

Figure 15 displays the repeat unit molecular volume^{48,49} V_m (including anion) dependence of the interpolated relaxation temperature $T_{\omega_{\max}}$ of the DRS α_2 , α , and α' and LVE α relaxations at $\omega_{\max} = 10$ rad/s. $T_{\omega_{\max}}$ of imidazolium-based PILs with various side chains decreases exponentially with increasing V_m and eventually levels off in the large V_m limit [see dashed (for DRS α , DRS α' , and LVE α) and solid (for DRS α_2) curves]. The dashed curve also describes T_g (from Figure 2), which decreases rapidly with increasing V_m and approaches a steady value in the large V_m limit, demonstrating that the segmental relaxation (α) involves the typical characteristics of the glass transition dynamics. Furthermore, in PILs with shorter side chains (smaller V_m) the relaxation temperatures for the α_2 process ($T_{\omega_{\alpha_2}}$) in DRS are lower than those for the α process (T_{ω_0}) in LVE and the α' process ($T_{\omega_{\alpha'}}$) in DRS, while PILs with longer side chains (larger V_m) exhibit higher $T_{\omega_{\alpha_2}}$ than $T_{\omega_{\alpha'}}$ and

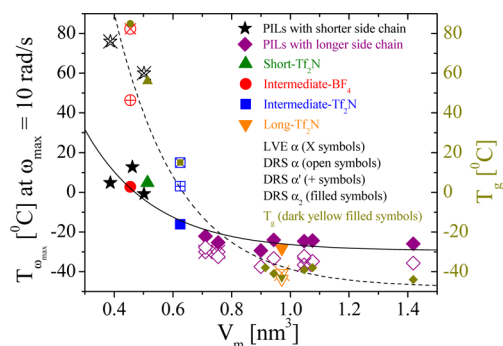


Figure 15. Correlation between relaxation temperature $T_{\omega_{max}}$ of the LVE α (× symbols), DRS α (open symbols), DRS α' (+ symbols), and DRS α_2 (filled symbols) relaxations (and T_g from Figure 2) and repeat unit molecular volume V_m (including the anion) for Long-Tf₂N, Intermediate-Tf₂N and -BF₄, and Short-Tf₂N. The data are taken from DRS and LVE measurements at a frequency of $\omega_{max} = 10$ rad/s. $T_{\omega_{max}}$ for imidazolium-based PILs with various side chains are also added from literature data: PILs with shorter side chains (black star symbols)^{20,28} and with longer side chain (purple diamond symbols).³² Solid (DRS α_2) and dashed (LVE α , DRS α , and DRS α') curves on $T_{\omega_{max}}$ are fits to guide the eye, using exponential curves, with the large V_m limit having $T_{\omega_{max}} = -29$ or -47 °C, respectively.

T_{ω_0} . This indicates that Intermediate-BF₄ and -Tf₂N exhibit slower polymer (α) motions than ion (α_2) motions, whereas for Long-Tf₂N the ion rearrangement (α_2) is slower than the polymer relaxation (α).

For longer side chains (highly diluted ions) where ions are temporarily localized in a certain domains, for ion motion over the scale of a few angstroms to occur, several rearrangements of the neighboring polymer segments must take place.³¹ This is why for Long-Tf₂N the α_2 process occurs at frequency $\sim 300\times$ lower than that of the α process, but with identical Vogel temperature. At higher ion content, we propose that *the ion domains become continuous, allowing ion motion (α_2) to be faster than the polymer motion (α)*. As a result, in the Intermediate-ionomers, the Vogel temperatures of the α_2 process from DRS are respectively 40 K (with BF₄[−] counterions) and 20 K (with Tf₂N[−] counterions) lower than those of the α process from LVE (see Table 5). Relaxation processes attributed to slowed-down segmental motion of complexed polymer segments have been observed for poly(propylene oxide) (PPO)–LiClO₄ mixtures.¹⁰⁶ In the dilute regime the “ion mode” (α_2) has been observed on the low-frequency side of the segmental mode (α), while at high salt concentration the segmental motion of PPO molecules has been significantly slowed down due to cation coordination.¹⁰⁶

I. Temperature Dependence of Ion Conduction and Polymer Relaxation. Conductivity is the product of charge e , number density of carriers p , and their mobility μ for single-ion conductors, so the temperature dependence of $\sigma_{DC}(T)$ shown in Figure 6 has already been evaluated by our Arrhenius fit of $p(T)$ to eq 8 in Figure 8 and our VFT fit of extended mobility $\mu(T) = \sigma_{DC}(T)/[ep(T)]$ to eq 9 in Figure 9:

$$\sigma_{DC} = e\mu_{\infty}p_{\infty} \exp\left(-\frac{DT_0}{T-T_0}\right) \exp\left(-\frac{E_a^p}{RT}\right) \text{ for } T > T_g$$

$$\sigma_{DC} = e\mu_{\infty}p_{\infty} \exp\left(-\frac{E_a^{\mu} + E_a^p}{RT}\right) \text{ for } T < T_g \quad (16)$$

Fits of eq 16 with parameters listed in Table 4 are shown as the solid curves in Figure 6. The fact that $\omega_{\alpha'}$, ω_{ω} , ω_{α_2} , μ , and σ_{DC} all share common T_0 demonstrates strong coupling between motion of counterions and polymer or ion dynamics. A vital point is that the VFT fit in Figure 9 to extended mobility data enables this conclusion because conductivity is measured with high precision very close to T_g . Consequently, the T_0 from extended mobility is the most precise and can give a good description of the temperature dependences of $\omega_{\alpha'}$, ω_{ω} , and ω_{α_2} . The DC conductivity can be also written using the Nernst–Einstein equation, $\mu = De/kT$, where D is the diffusion coefficient of charge carriers and kT is the thermal energy:³²

$$\sigma_{DC} = ep\mu = \frac{e^2 D p}{kT} \quad (17)$$

The Debye length $L_D \equiv [\epsilon_0 \epsilon_s kT / (e^2 p)]^{1/2}$ is the length scale over which thermal fluctuations allow ions to move. Our dielectric methods directly determine the time scale for this ion rearrangement, beyond which counterion motion becomes diffusive:

$$D = BL_D^2 \omega_{\alpha_2} = B \frac{\epsilon_0 \epsilon_s kT}{e^2 p} \omega_{\alpha_2} \quad (18)$$

where B is a constant. Then, putting this diffusion coefficient into eq 17, the DC conductivity can be written as

$$\sigma_{DC} = B \epsilon_0 \epsilon_s \omega_{\alpha_2} \quad (19)$$

This is a simple scaling correlation between ionic conductivity σ_{DC} and the product of dielectric constant ϵ_s and frequency at the loss maximum ω_{max} , originally proposed empirically by Barton, Nakajima, and Namikawa^{107–110} (BNN), who suggested that conduction and dielectric relaxation have their origins in one diffusion process. As shown in Figure 16, the conductivity can be successfully scaled in accordance with eq 19, further demonstrating that conductivity is strongly coupled with ion motion (the α_2 process). Furthermore, substitution of the time scale for conduction (eq 3) into eq 19 allows one to recognize that B is the ratio of time scale for ion rearrangement τ_{α_2} and conduction τ_{σ} :

$$B = \tau_{\alpha_2} / \tau_{\sigma} \quad (20)$$

Figure 16 demonstrates that B is a nonuniversal constant with values ranging from 0.4 to 32 (at least) for various single-ion conductors in the literature. In particular, the imidazolium-based PILs show correlation between B and molecular volume V_m (see inset of Figure 16). This indicates that the ion rearrangement time, relative to the time where counterion motion becomes diffusive, increases with increasing V_m .

CONCLUSIONS

This paper correlates morphology, viscoelasticity, ion conduction, and dielectric response of imidazolium-based single-ion conductors with different anions and with different side chain lengths. The effect of counterions is clearly observed in

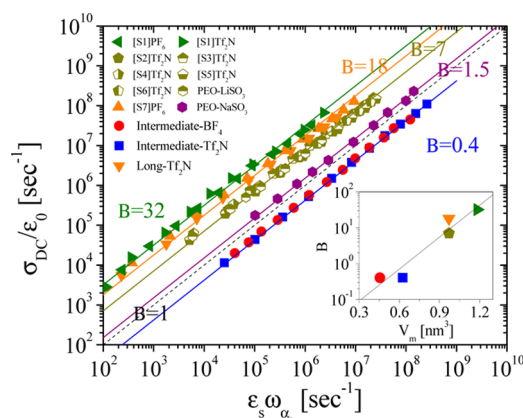


Figure 16. DC conductivity rate σ_{DC}/ϵ_0 vs the product of static dielectric constant ϵ_s and frequency ω_{α_2} of the α_2 process for TF_2N^- and BF_4^- ionomers, including literature data from refs 29, 31, and 32 for other single-ion conductors. The solid lines are fits of the BNN relation (eq 19) with $B = 0.4$ for Intermediate- BF_4 and $-\text{TF}_2\text{N}$ and $B = 18$ for Long- TF_2N , and the dashed line indicates eq 19 with $B = 1$. The inset shows B vs V_m for imidazolium-based PILs, and the solid line is an exponential fit to guide the eye.

the glass transition temperature and ionic conductivity; ionomers with TF_2N^- counterions have lower T_g s and higher ionic conductivities and ion mobilities than ionomers with BF_4^- counterions, as observed in X-ray scattering and viscoelastic measurements that show that the imidazolium cation is less prone to aggregation with TF_2N^- counterions than with BF_4^- counterions. The strong ion aggregation in the ionomer with BF_4^- counterions also significantly lowers the dielectric constant, reflected in the lower number density of simultaneously conducting ions.

The Intermediate side chain ionomers boost the ionic conductivity at T_g and have measurable conductivity below T_g with the Arrhenius character seen for inorganic glasses. The Long side chain dilutes ion content, lowers T_g , and allows ionic groups to more readily respond to the applied field, thereby raising the dielectric constant.

We propose that the PIL with Long side chains has insufficient number of ions to have continuous ion domains. This ionomer exhibits segmental (α) relaxation and $\sim 300\times$ slower ionic (α_2) relaxation in DRS, with a polymer segmental relaxation in LVE slightly slower than the α relaxation in DRS. The PILs with Intermediate side chains have continuous ion domains, exhibiting ionic (α_2) relaxation in DRS and significantly slower polymer relaxations in LVE, indicating that counterions transport without polymer motion, in the continuous ion domains. In all cases, the coupling between ion rearrangement (α_2) and conduction (σ_{DC}) is maintained, reflected in the same Vogel temperature for α_2 , μ , and σ_{DC} and the BNN relation between σ_{DC} and $\epsilon_s\omega_{\alpha_2}$ in each ionomer.

■ ASSOCIATED CONTENT

Supporting Information

DSC thermograms of Intermediate- BF_4 and $-\text{TF}_2\text{N}$ and Long- TF_2N ; a linear relationship between τ_{EP} and thickness L at 25 and 80 °C for Intermediate- TF_2N . This material is available free of charge via the Internet at <http://pubs.acs.org>.

■ AUTHOR INFORMATION

Corresponding Author

*E-mail rhc@plmsc.psu.edu (R.H.C.).

Notes

The authors declare no competing financial interest.

■ ACKNOWLEDGMENTS

This work is supported in part by the U.S. Army Research Office under Grant W911NF-07-1-0452 Ionic Liquids in Electro-Active Devices (ILEAD) MURI. We are grateful to Qiming Zhang and Quan Chen (both at Penn State) for helpful discussions.

■ REFERENCES

- (1) Ohno, H. *Electrochemical Aspects of Ionic Liquids*; John Wiley & Sons, Inc.: Hoboken, NJ, 2005.
- (2) Fukushima, T.; Asaka, K.; Kosaka, A.; Aida, T. *Angew. Chem., Int. Ed.* **2005**, *44*, 2410–2413.
- (3) Hapiot, P.; Lagrost, C. *Chem. Rev.* **2008**, *108*, 2238–2264.
- (4) Armand, M.; Endres, F.; MacFarlane, D. R.; Ohno, H.; Scrosati, B. *Nat. Mater.* **2009**, *8*, 621–629.
- (5) Ohno, H.; Ito, K. *Chem. Lett.* **1998**, 751–752.
- (6) Yoshizawa, M.; Ohno, H. *Chem. Lett.* **1999**, 889–890.
- (7) Snedden, P.; Cooper, A. I.; Scott, K.; Winterton, N. *Macromolecules* **2003**, *36*, 4549–4556.
- (8) Ohno, H.; Yoshizawa, M.; Ogihara, W. *Electrochim. Acta* **2004**, *50*, 255–261.
- (9) Washiro, S.; Yoshizawa, M.; Nakajima, H.; Ohno, H. *Polymer* **2004**, *45*, 1577–1582.
- (10) Nakajima, H.; Ohno, H. *Polymer* **2005**, *46*, 11499–11504.
- (11) Ogihara, W.; Suzuki, N.; Nakamura, N.; Ohno, H. *Polym. J.* **2006**, *38*, 117–121.
- (12) Ogihara, W.; Washiro, S.; Nakajima, H.; Ohno, H. *Electrochim. Acta* **2006**, *51*, 2614–2619.
- (13) Ohno, H. *Macromol. Symp.* **2007**, *249*, 551–556.
- (14) Green, M. D.; Long, T. E. *Polym. Rev.* **2009**, *49*, 291–314.
- (15) Xie, M.; Han, H.; Ding, L.; Shi, J. *Polym. Rev.* **2009**, *49*, 315–338.
- (16) Mecerreyes, D. *Prog. Polym. Sci.* **2011**, *36*, 1629–1648.
- (17) Yoshizawa, M.; Ohno, H. *Electrochim. Acta* **2001**, *46*, 1723–1728.
- (18) Ohno, H. *Electrochim. Acta* **2001**, *46*, 1407–1411.
- (19) Chen, H.; Choi, J.-H.; Salas-de la Cruz, D.; Winey, K. I.; Elabd, Y. A. *Macromolecules* **2009**, *42*, 4809–4816.
- (20) Nakamura, K.; Saiwaki, T.; Fukao, K. *Macromolecules* **2010**, *43*, 6092–6098.
- (21) Lee, M.; Choi, U. H.; Colby, R. H.; Gibson, H. W. *Chem. Mater.* **2010**, *22*, S814–S822.
- (22) Nakamura, K.; Saiwaki, T.; Fukao, K.; Inoue, T. *Macromolecules* **2011**, *44*, 7719–7726.
- (23) Green, M. D.; Salas-de la Cruz, D.; Ye, Y.; Layman, J. M.; Elabd, Y. A.; Winey, K. I.; Long, T. E. *Macromol. Chem. Phys.* **2011**, *212*, 2522–2528.
- (24) Weber, R. L.; Ye, Y.; Banik, S. M.; Elabd, Y. A.; Hickner, M. A.; Mahanthappa, M. K. *J. Polym. Sci., Part B: Polym. Phys.* **2011**, *49*, 1287–1296.
- (25) Weber, R. L.; Ye, Y.; Schmitt, A. L.; Banik, S. M.; Elabd, Y. A.; Mahanthappa, M. K. *Macromolecules* **2011**, *44*, 5727–5735.
- (26) Ye, Y.; Elabd, Y. A. *Polymer* **2011**, *52*, 1309–1317.
- (27) Salas-de la Cruz, D.; Green, M. D.; Ye, Y.; Elabd, Y. A.; Long, T. E.; Winey, K. I. *J. Polym. Sci., Part B: Polym. Phys.* **2012**, *50*, 338–346.
- (28) Nakamura, K.; Fukao, K.; Inoue, T. *Macromolecules* **2012**, *45*, 3850–3858.
- (29) Choi, U. H.; Lee, M.; Wang, S.; Liu, W.; Winey, K. I.; Gibson, H. W.; Colby, R. H. *Macromolecules* **2012**, *45*, 3974–3985.
- (30) Nakamura, K.; Fukao, K. *Polymer* **2013**, *54*, 3306–3313.

- (31) Fragiadakis, D.; Dou, S.; Colby, R. H.; Runt, J. *J. Chem. Phys.* **2009**, *130*, 064907.
- (32) Choi, U. H.; Mittal, A.; Price, T. L.; Gibson, H. W.; Runt, J.; Colby, R. H. *Macromolecules* **2013**, *46*, 1175–1186.
- (33) Register, R. A.; Prud'Homme, R. K. In *Ionomers*; Tant, M. R., Mauritz, K. A., Wikes, G. L., Eds.; Blackie Academic and Professional: London, 1997; pp 208–260.
- (34) Kremer, F.; Schönhals, A. *Broadband Dielectric Spectroscopy*; Springer-Verlag: New York, 2002.
- (35) Macdonald, J. R. *Phys. Rev.* **1953**, *92*, 4–17.
- (36) Coelho, R. *Rev. Phys. Appl.* **1983**, *18*, 137–146.
- (37) Barsoukov, E.; Macdonald, J. R. *Impedance Spectroscopy: Theory, Experiment, and Applications*; Wiley: New York, 2005.
- (38) Klein, R. J.; Zhang, S.; Dou, S.; Jones, B. H.; Colby, R. H.; Runt, J. *J. Chem. Phys.* **2006**, *124*, 144903.
- (39) Fragiadakis, D.; Dou, S.; Colby, R. H.; Runt, J. *Macromolecules* **2008**, *41*, 5723–5728.
- (40) Garcia, F.; Garcia-Bernabe, A.; Compan, V.; Diaz-Calleja, R.; Guzman, J.; Riande, E. *J. Polym. Sci., Part B: Polym. Phys.* **2001**, *39*, 286–299.
- (41) Floudas, G.; Stepanek, P. *Macromolecules* **1998**, *31*, 6951–6957.
- (42) Ishida, Y.; Yamafuji, K. *Kolloid Z.* **1961**, *177*, 97–116.
- (43) Sasabe, H.; Saito, S. *J. Polym. Sci., Part A-2* **1968**, *6*, 1401–1418.
- (44) Gaborieau, M.; Graf, R.; Kahle, S.; Pakula, T.; Spiess, H. W. *Macromolecules* **2007**, *40*, 6249–6256.
- (45) Heiney, P. A. *Comm. Powder Diffr. Newsl.* **2005**, *32*, 9–11.
- (46) van Krevelen, D. W. *Properties of Polymers*; Elsevier: New York, 1990.
- (47) Fernicola, A.; Scrosati, B.; Ohno, H. *Ionics* **2006**, *12*, 95–102.
- (48) Slattery, J. M.; Daguene, C.; Dyson, P. J.; Schubert, T. J. S.; Krossing, I. *Angew. Chem., Int. Ed.* **2007**, *46*, 5384–5388.
- (49) The molecular volumes are calculated from the group contribution method⁴⁶ or are taken from ref 48.
- (50) Liu, W.; Janik, M. J.; Colby, R. H. In *Polymers for Energy Storage and Delivery: Polyelectrolytes for Batteries and Fuel Cells*; Page, K. A., Soles, C. L., Runt, J., Eds.; American Chemical Society: Washington, DC, 2011; pp 19–44.
- (51) Annapureddy, H. V. R.; Kashyap, H. K.; De Biase, P. M.; Margulis, C. J. *J. Phys. Chem. B* **2010**, *114*, 16838–16846.
- (52) Kashyap, H. K.; Santos, C. S.; Annapureddy, H. V. R.; Murthy, N. S.; Margulis, C. J.; Castner, E. W. *Faraday Discuss.* **2012**, *154*, 133–143.
- (53) Kashyap, H. K.; Hettige, J. J.; Annapureddy, H. V. R.; Margulis, C. J. *Chem. Commun.* **2012**, *48*, 5103–5105.
- (54) Wang, W.; Liu, W.; Tudryn, G. J.; Colby, R. H.; Winey, K. I. *Macromolecules* **2010**, *43*, 4223–4229.
- (55) The electron densities of counterions (BF₄ and Tf₂N), cation [1-butyl-3-methylimidazolium (C₄MIM)], and nonionic part of the ionomers (Intermediate- and Longest-ionomers) have been estimated: BF₄ (0.933 mol cm⁻³), Tf₂N (0.981 mol cm⁻³), C₄MIM (0.653 mol cm⁻³), nonionic part of the Intermediate-ionomer (0.915 mol cm⁻³), and nonionic part of the Longest-ionomer (0.881 mol cm⁻³). The fact that the electron density of BF₄ matches that of nonionic part of the Intermediate-ionomer explains why the BF₄⁻ ionomer does not display a *q*_{II} scattering peak.
- (56) Wang, W.; Tudryn, G. J.; Colby, R. H.; Winey, K. I. *J. Am. Chem. Soc.* **2011**, *133*, 10826–10831.
- (57) Peiffer, D. G.; Weiss, R. A.; Lundberg, R. D. *J. Polym. Sci., Part B: Polym. Phys.* **1982**, *20*, 1503–1509.
- (58) Weiss, R. A.; Agarwal, P. K.; Lundberg, R. D. *J. Appl. Polym. Sci.* **1984**, *29*, 2719–2734.
- (59) Galambos, A. F.; Stockton, W. B.; Koberstein, J. T.; Sen, A.; Weiss, R. A.; Russell, T. P. *Macromolecules* **1987**, *20*, 3091–3094.
- (60) Fitzgerald, J. J.; Weiss, R. A. *J. Macromol. Sci., Rev. Macromol. Chem.* **1988**, *C28*, 99–185.
- (61) Semenov, A. N.; Joanny, J.-F.; Khokhlov, A. R. *Macromolecules* **1995**, *28*, 1066–1075.
- (62) Colby, R. H.; Zheng, X.; Rafailovich, M. H.; Sokolov, J.; Peiffer, D. G.; Schwarz, S. A.; Strzhemechny, Y.; Nguyen, D. *Phys. Rev. Lett.* **1998**, *81*, 3876–3879.
- (63) Weiss, R. A.; Yu, W.-C. *Macromolecules* **2007**, *40*, 3640–3643.
- (64) Weiss, R. A.; Zhao, H. *J. Rheol.* **2009**, *53*, 191–213.
- (65) Tudryn, G. J.; Liu, W.; Wang, S.-W.; Colby, R. H. *Macromolecules* **2011**, *44*, 3572–3582.
- (66) Vanhoorne, P.; Register, R. A. *Macromolecules* **1996**, *29*, 598–604.
- (67) Tierney, N. K.; Register, R. A. *Macromolecules* **2002**, *35*, 2358–2364.
- (68) Tierney, N. K.; Register, R. A. *Macromolecules* **2003**, *36*, 1170–1177.
- (69) Rubinstein, M.; Colby, R. H. *Polymer Physics*; Oxford University Press: London, 2003.
- (70) Weiss, R. A.; Fitzgerald, J. J.; Kim, D. *Macromolecules* **1991**, *24*, 1071–1076.
- (71) Kawasaki, Y.; Watanabe, H.; Uneyama, T. *Nihon Reorogi Gakkaishi* **2011**, *39*, 127–131.
- (72) Chen, Q.; Tudryn, G. J.; Colby, R. H. *J. Rheol.* **2013**, *57*, 1441–1462.
- (73) Williams, M. L.; Landel, R. F.; Ferry, J. D. *J. Am. Chem. Soc.* **1955**, *77*, 3701–3707.
- (74) Mark, J. E.; Eisenberg, A.; Graessley, W. W.; Mandelken, L.; Koenig, J. L. *Physical Properties of Polymers*; American Chemical Society: Washington, DC, 1984.
- (75) Tokuda, H.; Hayamizu, K.; Ishii, K.; Susan, M. A. B. H.; Watanabe, M. *J. Phys. Chem. B* **2005**, *109*, 6103–6110.
- (76) Kawamura, J.; Shimoji, M. *Mater. Chem. Phys.* **1989**, *23*, 99–120.
- (77) Williams, S. R.; Borgerding, E. M.; Layman, J. M.; Wang, W.; Winey, K. I.; Long, T. E. *Macromolecules* **2008**, *41*, 5216–5222.
- (78) Williams, S. R.; Salas-de la Cruz, D.; Winey, K. I.; Long, T. E. *Polymer* **2010**, *51*, 1252–1257.
- (79) Kawamura, J.; Shimoji, M. *J. Non-Cryst. Solids* **1986**, *88*, 281–294.
- (80) Canongia Lopes, J. N. A.; Padua, A. A. H. *J. Phys. Chem. B* **2006**, *110*, 3330–3335.
- (81) Wang, Y.; Voth, G. A. *J. Am. Chem. Soc.* **2005**, *127*, 12192–12193.
- (82) Coelho, R. *J. Non-Cryst. Solids* **1991**, *131*, 1136–1139.
- (83) Coelho, R. *Physics of Dielectrics for the Engineer*; Elsevier: New York, 1979.
- (84) When we use the asymmetric function from the Macdonald model³¹ for electrode polarization (EP), the slope on the high-frequency side of EP is nearly quantitatively identical to that of a simpler power law. In order to reduce the number of overall fitting parameters and to achieve more stable fits, we therefore set the high-frequency slope to 1.9 in the fit of derivative spectra.
- (85) Wang, S.-W.; Liu, W.; Colby, R. H. *Chem. Mater.* **2011**, *23*, 1862–1873.
- (86) At infinite temperature, all aggregates would presumably be broken and the expectation would be $p_{\infty} = p_0$. In our system, we interpret the apparent p_{∞} to be the nontrapped ions participating in conduction at temperatures studied.
- (87) Onsager, L. *J. Am. Chem. Soc.* **1936**, *58*, 1486–1493.
- (88) Botcher, C. J. F. *Theory of Electric Polarization*; Elsevier: Amsterdam, 1973; Vol. 1.
- (89) Saito, S.; Nakajima, T. *J. Appl. Polym. Sci.* **1959**, *2*, 93–99.
- (90) Saito, S.; Nakajima, T. *J. Polym. Sci.* **1959**, *37*, 229–240.
- (91) Lavina, S.; Negro, E.; Pace, G.; Gross, S.; Depaoli, G.; Vidali, M.; Di Noto, V. *J. Non-Cryst. Solids* **2007**, *353*, 2878–2888.
- (92) Williams, G. *Trans. Faraday Soc.* **1963**, *59*, 1397–1413.
- (93) Wübbenhorst, M.; van Turnhout, J. *J. Non-Cryst. Solids* **2002**, *305*, 40–49.
- (94) Boersma, A.; van Turnhout, J.; Wübbenhorst, M. *Macromolecules* **1998**, *31*, 7453–7460.
- (95) Diaz-Calleja, R. *Macromolecules* **2000**, *33*, 8924–8924.

- (96) Weingärtner, H.; Sasisanker, P.; Daguene, C.; Dyson, P. J.; Krossing, I.; Slattery, J. M.; Schubert, T. *J. Phys. Chem. B* **2007**, *111*, 4775–4780.
- (97) Hunger, J.; Stoppa, A.; Schrödle, S.; Hefter, G.; Buchner, R. *ChemPhysChem* **2009**, *10*, 723–733.
- (98) Strobl, G. R. *The Physics of Polymers: Concepts for Understanding Their Structures and Behavior*, 3rd ed.; Springer: New York, 2007.
- (99) McCrum, N. G.; Read, B. E.; Williams, G. *Anelastic and Dielectric Effects in Polymeric Solids*; Dover: New York, 1967.
- (100) Alper, T.; Barlow, A. J.; Gray, R. W. *Polymer* **1976**, *17*, 665–669.
- (101) Colmenero, J.; Alegria, A.; Santangelo, P. G.; Ngai, K. L.; Roland, C. M. *Macromolecules* **1994**, *27*, 407–410.
- (102) Pakula, T.; Geyler, S.; Edling, T.; Boese, D. *Rheol. Acta* **1996**, *35*, 631–644.
- (103) Santangelo, P. G.; Roland, C. M. *Macromolecules* **1998**, *31*, 3715–3719.
- (104) Leibler, L.; Rubinstein, M.; Colby, R. H. *Macromolecules* **1991**, *24*, 4701–4707.
- (105) Chen, Q.; Liang, S.; Shiau, H.-S.; Colby, R. H. *ACS Macro Lett.* **2013**, *2*, 970–974.
- (106) Furukawa, T.; Mukasa, Y.; Suzuki, T.; Kano, K. *J. Polym. Sci., Part B: Polym. Phys.* **2002**, *40*, 613–622.
- (107) Namikawa, H. *J. Non-Cryst. Solids* **1974**, *14*, 88–100.
- (108) Namikawa, H. *J. Non-Cryst. Solids* **1975**, *18*, 173–195.
- (109) Dyre, J. C. *Phys. Rev. B* **1993**, *48*, 12511–12526.
- (110) Macdonald, J. R. *J. Appl. Phys.* **2010**, *107*, 101101.